Multispecies model of cell lineages and feedback control in solid tumors

Supplementary Material

H. Youssefpour[1], X. Li[2], A.D. Lander[3, 4], J.S. Lowengrub[1, 2, 4]

1. Department of Chemical Engineering and Materials Science, University of California, Irvine
2. Department of Mathematics, University of California, Irvine
3. Department of Developmental and Cell Biology, University of California, Irvine
4. Department of Biomedical Engineering, University of California, Irvine

In the following, all equation numbers and figure citations without "S" refer back to equations and figures in the main text.

S1. Numerical method

To solve the governing equations (18)-(31) efficiently, an adaptive finite difference-nonlinear multigrid method is developed following previous work by Wise et al. (2008, 2011). In this approach, the high-order system after time discretization is rewritten as a larger system of 2nd order elliptic equations. We only solve for ϕ_T, ϕ_{CSC} and ϕ_{DC}; the TCs and host volume fractions are found by $\phi_{TC} = \phi_T - \left(\phi_{CSC} + \phi_{DC}\right)$ and $\phi_H = 1 - \phi_T$ respectively.

An implicit 2nd order accurate time discretization of Crank-Nicholson type is used to remove the high-order time step constraint (e.g., $\Delta t \approx h^4$, where Δt and h are the time and spatial grid sizes) that would be incurred by an explicit method. Instead, our implicit method is found to be stable with $\Delta t \approx h$. Spatial derivatives are discretized using 2nd order accurate central difference approximations. Block structured Cartesian refinement is used to provide enhanced local resolution in regions where large gradients develop. Each level of refinement consists of a collection of Cartesian mesh patches with grid sizes equal to one half of the parent mesh. The nonlinear equations at the implicit time level are solved using a nonlinear, multilevel multigrid method. We refer the reader to Wise et al. (2008, 2011) for further details.

We solve the 2D system of equations in the square computational domain $[-20,20]^2$. The time step is $\Delta t=0.005$. The coarsest level mesh (root level 0) uses 64x64 grid points with corresponding grid size $h_0=0.625$. We use three levels of mesh refinement with grid sizes $h_1=0.3125$, $h_2=0.15625$ and $h_3=0.078125$ respectively. For the 3D system the computational domain is $[-10,10]^3$, the time step is $\Delta t=0.005$, the coarsest mesh is 32x32x32 with grid size $h_0=0.625$ and there are two levels of refinement with grid sizes $h_1=0.3125$ and $h_2=0.15625$.

The finest mesh gives the effective resolution of the simulation. Due to mesh adaptivity, this high resolution is obtained at a fraction of the cost of using this high resolution uniformly throughout the whole domain. After extensive testing, we found it sufficient to resolve gradients in ϕ_T here. This is because in all of the simulations presented in this

paper, the fine mesh covers the entire tumor and thus also resolves the concentrations of O, T, W and WI within the tumor and the volume fractions of the tumor constituents. This is illustrated in Fig. S1 where the adaptive mesh, together with the contours of ϕ_T, are shown at a late time after a growing tumor has broken apart. This corresponds to the simulation shown in Fig. 2 at time t=1000 (see Sec. 4.1in the main text for the parameters).

S2. Effect of the initial tumor shape on 2D tumor progression

Because of the importance of spatial effects on feedback regulation and tumor progression, we next examine the evolution from a non-circular initial tumor morphology. We consider two strengths of feedback response $\Psi = 1.0$ and $\Psi = 2.0$ and we consider two different non-circular initial tumor morphologies—an ellipse with aspect ratio slightly greater than one (a=4, b=3 in Eq. (32)) and a more elongated ellipse with a larger aspect ratio (a=10, b=1 in Eq. (32)). All other parameters are the same as in Tables 1-6 and the initial data for C_W and C_{WI} are as before. The results are presented in Fig. S2 showing the total volume of the tumor and the corresponding tumor morphologies (contours of ϕ_{TC}) respectively. For reference, the results using an initially circular tumor are also shown. When $\Psi = 1.0$, the initial elliptical tumor grows more rapidly than its circular counterpart. The corresponding morphology is also more complex. When $\Psi = 2.0$, the stronger feedback response suppresses shape perturbations. The initially elliptical tumor becomes nearly circular and evolves very similarly to its circular counterpart, which may become unstable at a much later time. However, when the elongated ellipse is used as the initial condition for this case ($\Psi = 2.0$), its evolution deviates from the circular case as the shape perturbation grows. This illustrates that the regulation of tumor progression by feedback control is sensitive to the tumor morphology since changes in tumor shape affect the spatiotemporal distribution of feedback factors.

S3. The effect of cell-cell adhesion

We next consider the effect of cell-cell adhesion on tumor progression through the parameter γ in Eq. (21). Like a surface tension, this parameter controls the stiffness of the tumor boundary with larger values corresponding to stiffer boundaries. In Fig. S3, results are shown for different values of γ for the fixed feedback parameter Ψ=0.1. The remaining parameters are listed in Tables 1-6, and G is given by Eq. (35). As γ is increased, the tumor grows much more slowly (Fig. S3(a)) and with a more compact morphology (Fig. S3(b)). Increasing the stiffness γ of the boundary leads to longer plateaus of nearly unchanging tumor volume after which morphological instability occurs and the volume increases concomitantly. There still does not appear to be a stable steady state even in the γ=0.5 case since the tumor still grows albeit at a slow rate and instability may be expected to occur at a much later time. Additional investigations should be performed to determine the behavior at even larger values of γ. Note that increasing γ induces time step restrictions for the stability of the algorithm making the computation

more expensive, although the use of new unconditionally stable algorithms (e.g., S.M. Wise (2010), J. Sci. Comput., v. 44, 38-68) can alleviate much of this expense.

S4. The effect of varying the *W* source u_0

We next consider the effect of the *W* source u_0 in Eq. (30). In Fig. S4, we plot the evolution of a tumor (TC contours) with u_0=1 and the cut-off function $G = 1$. All other parameters are as in Figs. 2 and 7, where u_0=0.2. Observe that the tumor grows much more rapidly and the tumor develops a stronger morphological instability than that shown in Fig. 7(d), which shows the corresponding case with G =1 and u_0=0.2. In addition, the number of CSC clusters increases from 6 to 7 at early times, and continues to increase throughout the progression of the tumor, resulting in a bumpy morphology with invasive fingers.

S5. Nutrient-independent *W* and *WI* production

In order to study the consequences of the *O*-dependent production of *W* and *WI* on tumor progression, we set C_O=1 in the source terms in Eqs. (30) and (31) so that production of *W* and *WI* are independent of the oxygen level. All other parameters, and the initial data, are the same as in Fig. 2. The results are shown in Fig. S5. In Fig. S5(a), the tumor volumes and the total volume fraction of the tumor components are plotted as a function of time. Observe that the progression is much more stable than that found in Fig. 2 with the evolution reaching a long plateau of nearly constant volume. The CSC, TC and DC fractions are roughly similar to that in Fig. 5; the CSC volume seems to slightly increase and CSCs comprise a slightly higher fraction of the tumor compared to that in Fig. 2. Thus, the tumor may become unstable at a much later time. This is under investigation.

In Figs. S5(b) and (c), the ϕ_T=0.5 and ϕ_{CSC}=0.4 contours are shown together with the contours of the self-renewal fraction P_0 and the concentrations C_W, C_O and C_T, respectively. The CSC clusters are now located much farther from the tumor boundary than was the case in Fig. 2. Correspondingly, the *O* level is quite low and thus the overall proliferation rate of the CSC is significantly lower from that in Fig. 2. The concentration C_W and self-renewal fraction P_0 nearly co-localize with the CSC clusters, while C_T is nearly uniform across the CSC cluster. Thus, the proliferation of CSCs is nearly uniform (and low) across the CSC cluster. This serves to enhance stability and thus the tumor remains roughly circular in contrast to the case in Fig. 2. This suggests that the asymmetry in self-renewal fraction introduced by the *O*-dependent production of *W* and *WI* is responsible for tumor instability.

S6. Advective transport of *W* and *WI*

We finally investigate the effect of advective transport of W and WI. That is, in Eqs. (28) and (29), the terms $\nabla \cdot \left(\mathbf{u}_s C_W \right)$ and $\nabla \cdot \left(\mathbf{u}_s C_{WI} \right)$ are retained. The resulting tumor progression is shown in Figs. S6(a) and (b) with the same parameters as used in Fig. 2 in the main text. Fig. S6(a) shows the volume fractions ϕ_{TC} and should be compared with Fig. 2(b). Note that the evolution is very similar to the case without advection with

3

differences between the two arising only after time $t = 600$ when the tumor breaks up into fragments and begins to grow very rapidly. This is further confirmed by Fig. S6(b), which shows the volumes of the tumor components. The thick lines indicate the simulation with advective transport shown in Fig. S6(a). Thus, we conclude that while advective transport of W and WI may influence the detailed tumor morphologies after the tumor breaks up, the overall evolution is very similar to the case without advective transport.
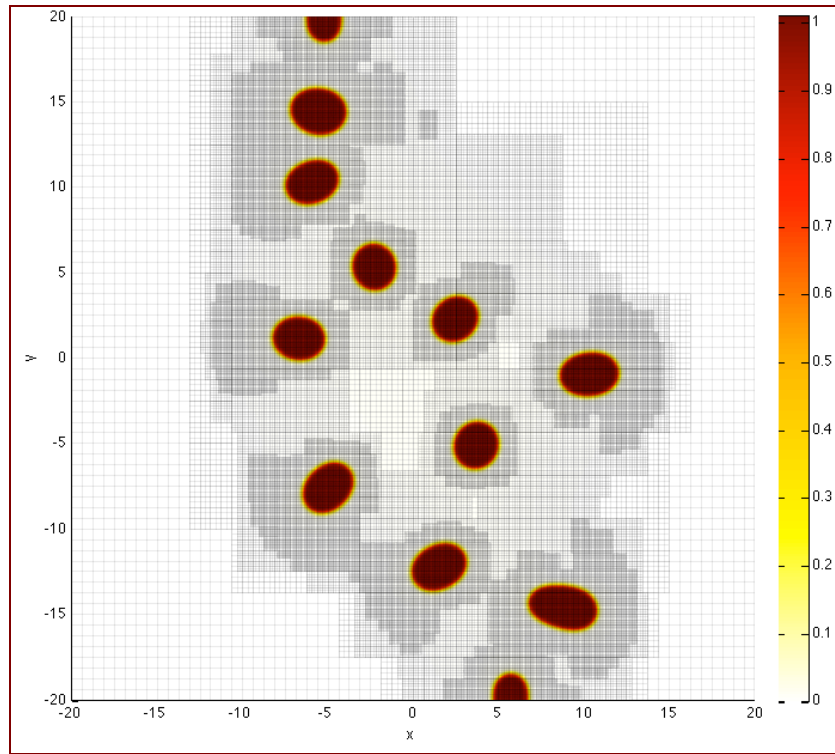
Figure S1. Adaptive mesh refinement enhances the local resolution of a growing tumor. Here, the refined mesh patches cover the tumor fragments that formed during growth. The simulation corresponds to that shown in Fig. 2 at time $t = 1000$. Colors online.
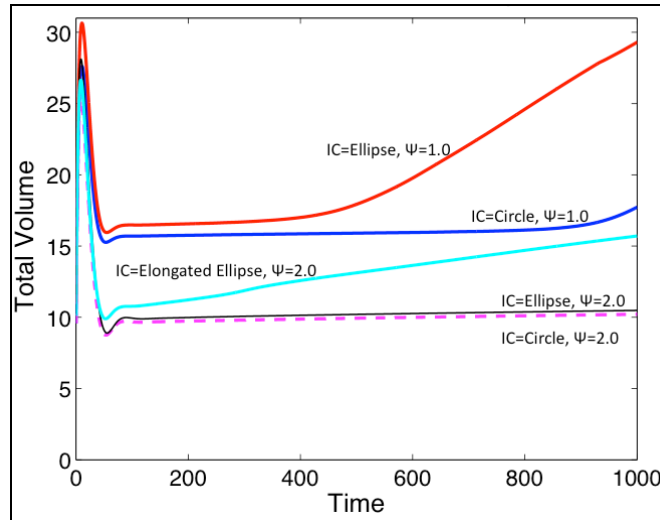
(a)
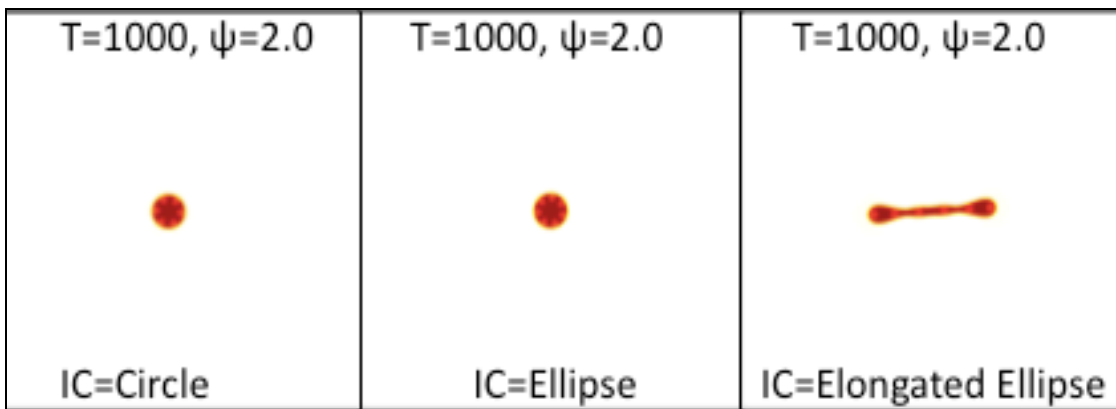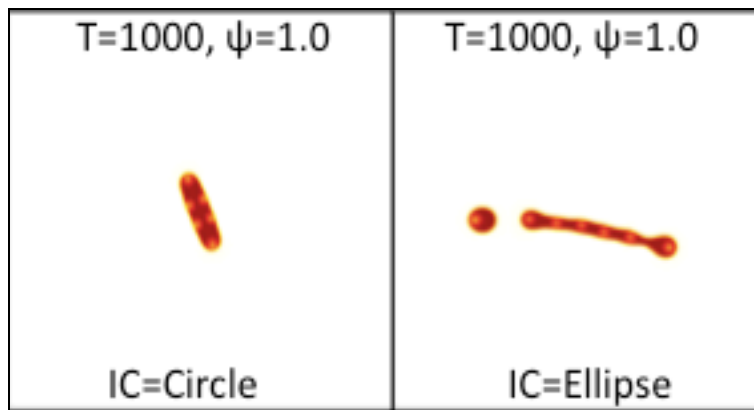
(b)

Figure S2. The initial tumor shape affects progression and response to feedback regulation. In (a), the volumes of tumors with different initial shape are plotted as marked. See text for details. In (b), the corresponding tumor morphologies (contours of ϕ_{TC}) are shown. Colors online.
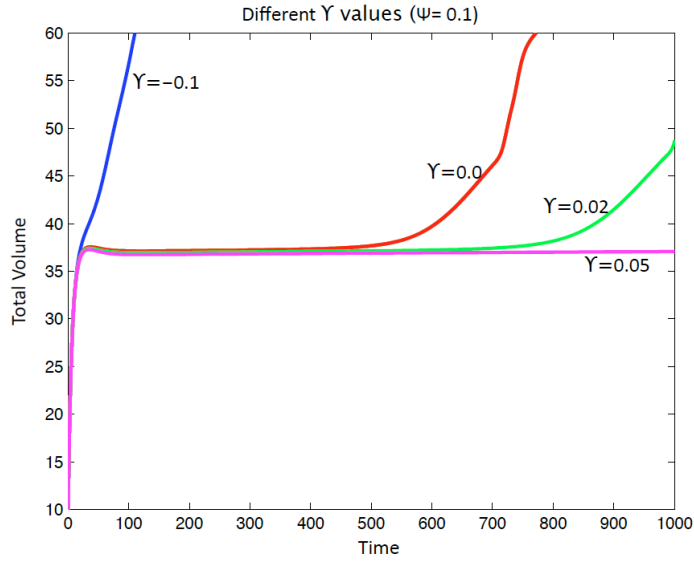
(a)
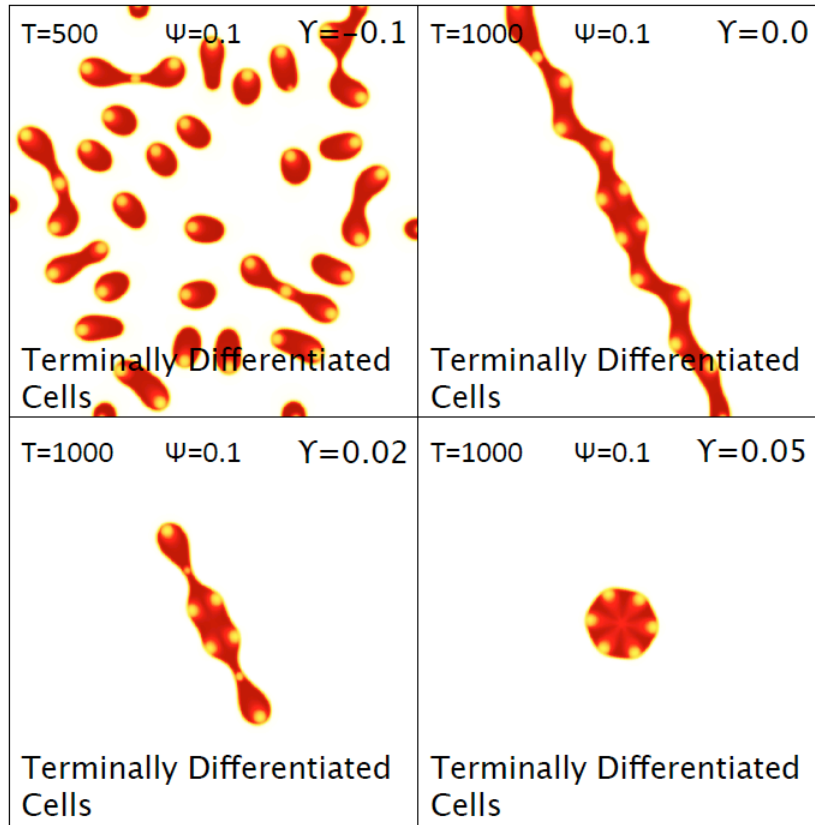
(b)

Figure S3. The effect of cell-cell adhesion on tumor progression with feedback strength Ψ=0.1. (a) Evolution of tumor volumes for different adhesion strength γ as indicated. (b) Associated tumor morphologies (contours of ϕ_{TC}) at time t =1000, as labeled. Colors online.
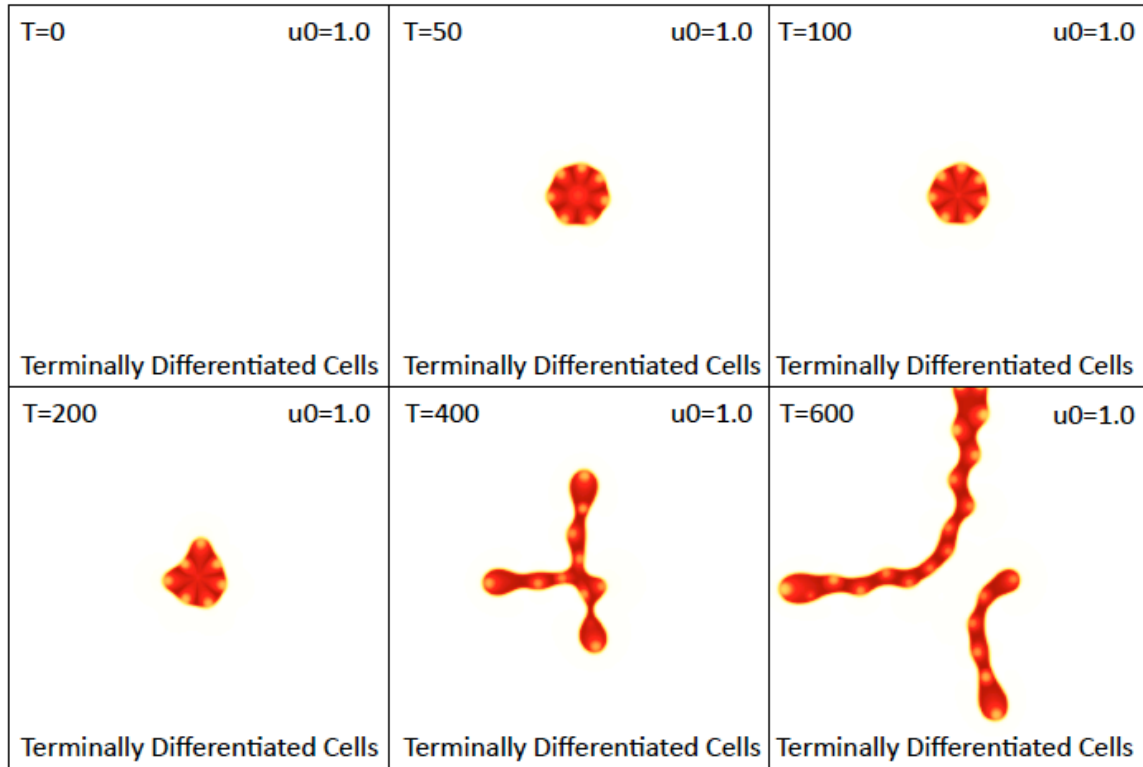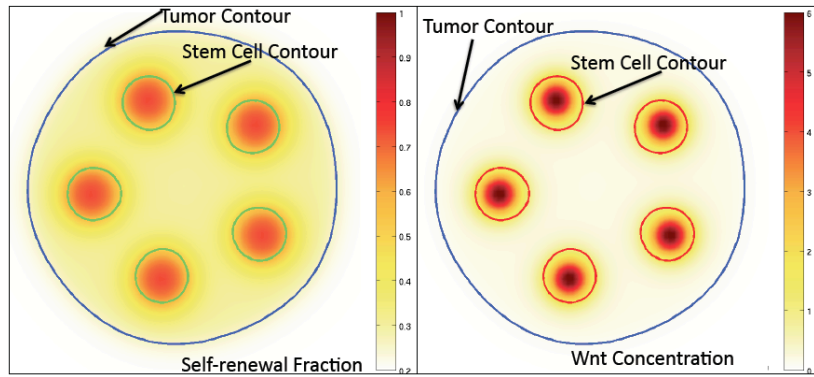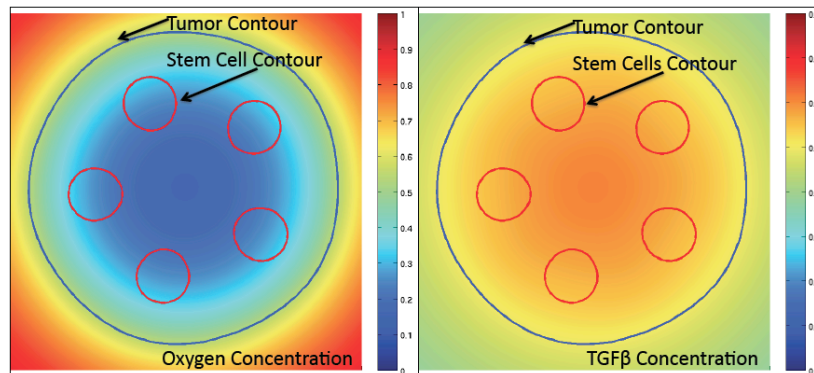
Figure S4. The background level of *W* production affects the tumor growth rate and the number of CSC clusters. Increasing u_0 to 1 (from $u_0=0.2$, as in Fig. 7(d)), increases the tumor size, the number of SC clusters and invasiveness. Colors online.
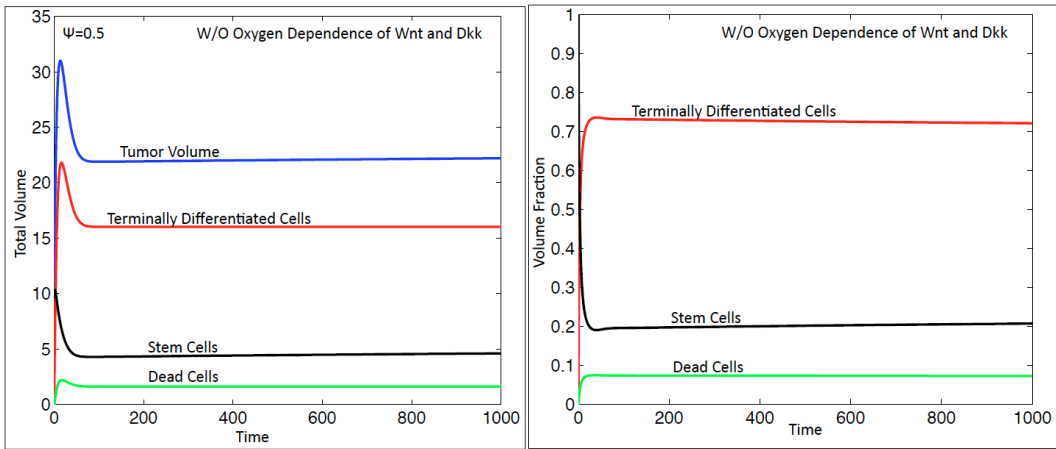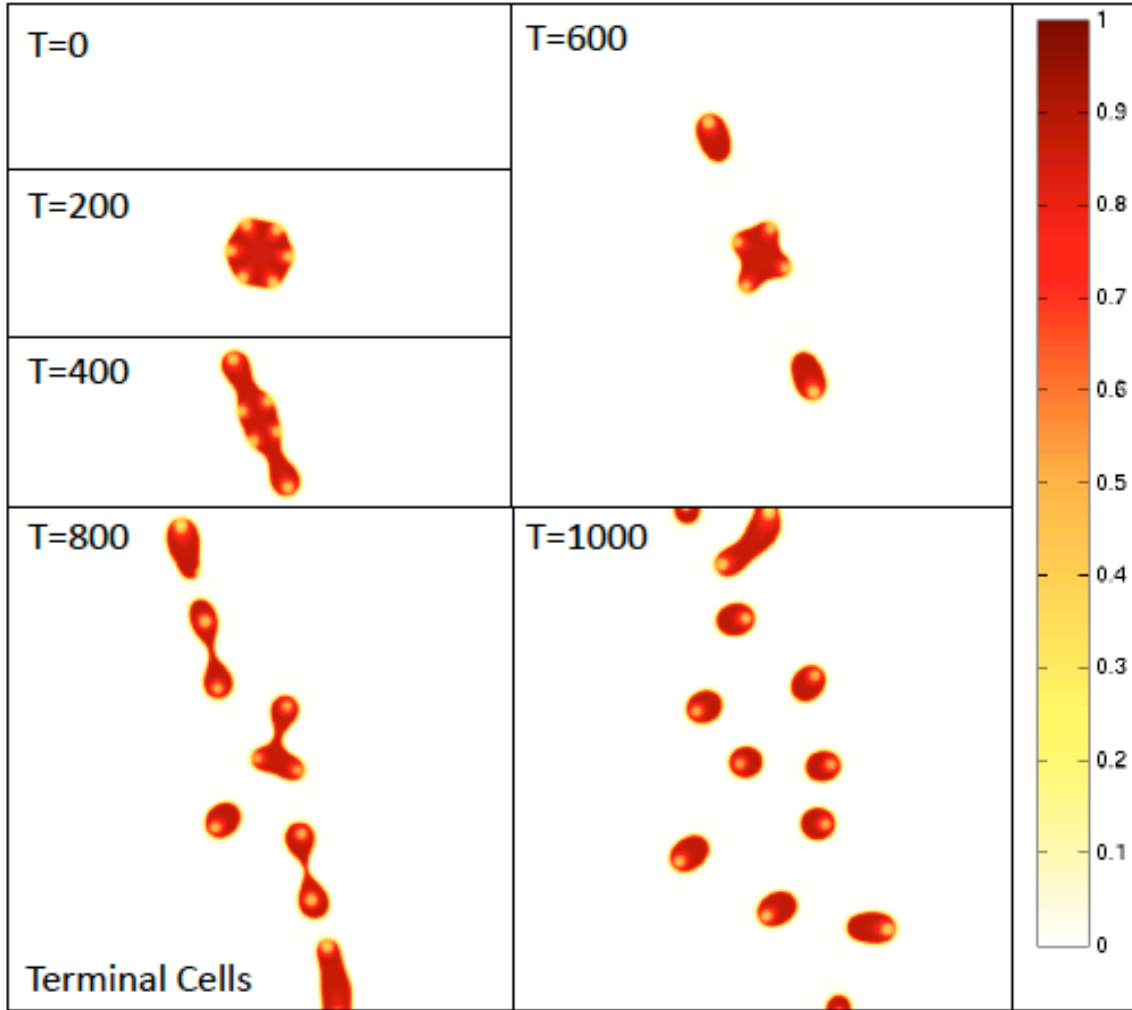
Figure S5. Tumor progression with O-independent production of W and WI. (a) The volume (left) and the total volume fraction (right) of the tumor and its components. (b) The self-renewal fraction (left) and the W concentration (right). (c) The O concentration (left) and the T concentration (right). In (b) and (c), the ϕ_T=0.5 and ϕ_{CSC}=0.4 contours at time t =1000 are also shown. Colors online.

9

(a)

Figure S6. Tumor progression with advection transport of *W* and *WI*. (a) The contours of the volume fraction of ϕ_{TC} at the times indicated (colors online); compare to Fig. 2(b) for case without advective transport.
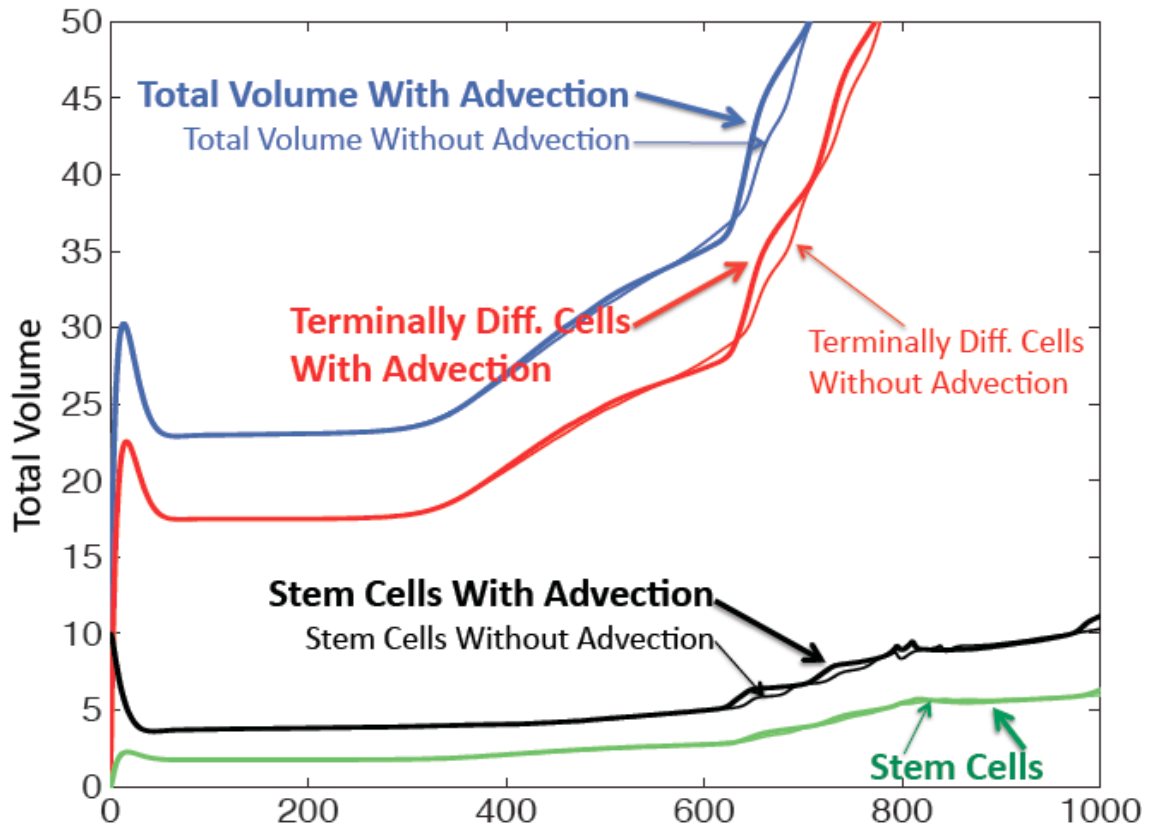
Figure S6. (b). The time evolutions of the volumes of the tumor components, as labeled. Thick lines correspond to the case with advective transport of *W* and *WI*.